THE ASTROPHYSICAL JOURNAL, 543:1016–1026, 2000 November 10

ANALYSIS OF A SOLAR ACTIVE REGION EXTREME-ULTRAVIOLET SPECTRUM FROM SERTS-97

JEFFREY W. BROSIUS,[1] ROGER J. THOMAS, AND JOSEPH M. DAVILA
Code 682, NASA Goddard Space Flight Center, Greenbelt, MD 20771

AND

ENRICO LANDI
Max-Planck-Institut für Aeronomie, Postfach 2, D-37191 Katlenburg-Lindau, Germany
Received 2000 April 6; accepted 2000 May 22

ABSTRACT

Goddard Space Flight Center's Solar EUV Research Telescope and Spectrograph was flown on 1997 November 18, carrying an intensified CCD detector and a multilayer-coated toroidal diffraction grating with enhanced sensitivity over that of a standard gold-coated grating throughout the instrument's 299–353 Å spectral bandpass. Spectra and spectroheliograms of NOAA Active Region 8108 (N21°, E18°) were obtained with a spectral resolution (instrumental FWHM) of 115 mÅ. Nearly 100 emission lines were observed in the spatially averaged active region spectrum. Spectra and spectroheliograms of quiet areas south of the region were also obtained. An end-to-end radiometric calibration of the rocket instrument was carried out at the Rutherford-Appleton Laboratory in the same facility that was used to calibrate the Coronal Diagnostic Spectrometer experiment on *SOHO* and using the same EUV light source. The accuracy of this calibration is confirmed by the excellent agreement between the measured and theoretical values of density- and temperature-insensitive line intensity ratios. Nine emission lines of Fe XV are identified in our spectrum; however, large differences between wavelengths in the CHIANTI database and some of the measured solar wavelengths, as well as inconsistencies of various theoretical intensity ratios, suggest a need for improvement in the Fe XV atomic physics parameters and/or the presence of unidentified blending lines. Density-sensitive line intensity ratios of Fe XI $\lambda\lambda$308.55/352.67, Fe XII $\lambda\lambda$338.27/352.11, Fe XIII $\lambda\lambda$320.80/312.17, and Fe XV $\lambda\lambda$321.78/327.03 yield logarithmic electron densities (in cm^{-3}) of 9.92 ± 0.28, 9.74 ± 0.28, 9.52 ± 0.30, and 9.62 ± 0.26, respectively. Using the strongest emission line observed for each ionization stage of Fe from X through XVI and Ni XVIII, we find that all of the measured nonthermal line widths yield velocities consistent with 35 km s^{-1}. The differential emission measure curve derived from the observed line intensities exhibits a relative minimum at $\log T \sim 5.7$, a broad maximum centered around $\log T \sim 6.3$, and a rapid decline for temperatures above $\log T \sim 6.6$.

Subject headings: instrumentation: spectrographs — line: identification — Sun: activity — Sun: corona — Sun: UV radiation

1. INTRODUCTION

Reliable measurements of the density, emission measure, mass motion, filling factor, and magnetic field strength are essential for understanding the multithermal structures in the solar corona and to determine the physical processes occurring therein. The extreme-ultraviolet (EUV) waveband (150–1200 Å) contains emission lines formed at temperatures ranging from several times 10^4 K to several times 10^7 K and is therefore well suited for studies of those multithermal coronal structures. This is why the EUV waveband was chosen for the Goddard Space Flight Center's (GSFC) Solar EUV Research Telescope and Spectrograph (SERTS) as well as for the Coronal Diagnostic Spectrometer (CDS) aboard the NASA/ESA *SOHO* spacecraft.

Previous solar EUV observations obtained with the Harvard scanning spectrometer on *OSO*-6 (Dupree et al. 1973), the EUV and X-ray spectroheliograph on *OSO*-7 (Neupert, Thomas, & Chapman 1974), and the EUV spectrometer-spectroheliometer on *Skylab* (Vernazza & Reeves 1978) had such coarse spectral resolution ($\sim$0.8 Å or greater) that they precluded accurate determinations of coronal plasma properties from line-ratio measurements in most cases. However, their spatial resolution was adequate to separate active from quiet areas and enabled them to suggest that temperatures at least as high as 2.5×10^6 K occur in quiet-Sun areas (Vernazza & Reeves 1978). It also allowed them to find that the higher the temperature of line formation, the greater the enhancement of the active region compared to quiet-Sun intensity (Dupree et al. 1973). Behring et al. (1976) obtained spectra with 0.06 Å spectral resolution, which have proved very useful for providing line identifications at EUV wavelengths. However, those spectra were acquired from full-Sun observations and so provide no information about distinct features on the Sun. Further, the relative line intensities were only approximately calibrated, rendering line intensity ratio measurements inaccurate. Malinovsky & Heroux (1973) obtained EUV spectra with a modest resolution (FWHM of the instrumental line shape $\sim$0.25 Å) during a sounding rocket flight. The estimated accuracy of their absolute intensities varies from 20% to 50% depending on the ratio of the line intensity to background; however, no corrections for atmospheric absorption were applied. Further, the Malinovsky & Heroux (1973) spectrum was acquired from full-Sun observations and so provides no information about distinct solar features. Observations obtained with the Naval Research Laboratory (NRL) slitless spectrograph on *Skylab* (Tousey et al. 1977) provided high spatial ($\sim$2″) and spectral ($\sim$0.1 Å) resolution images in the 171–630 Å waveband but were limited by the overlap of images from nearby spectral lines. They provided excellent diagnostic capabilities for small,

[1] Raytheon ITSS, 4400 Forbes Boulevard, Lanham, MD 20706.

intense sources like flares (e.g., Dere 1978; Dere et al. 1979) but were less than ideal for quiet-Sun areas and quiescent active regions.

SERTS was designed to improve on the earlier solar EUV instrumentation by (1) retaining the stigmatic imaging capability of the NRL spectroheliograph on *Skylab* (Tousey et al. 1977) while providing a spatial selection capability that reduces image overlap, and (2) achieving high spectral resolution. The version of SERTS that was flown in 1989 (SERTS-89; Neupert et al. 1992; Thomas & Neupert 1994; Young, Landi, & Thomas 1998) carried a standard gold-coated toroidal diffraction grating. It observed hundreds of first-order emission lines between 235 and 450 Å as well as dozens of second-order lines between 170 and 225 Å. The version of SERTS flown in 1991 (SERTS-91; Brosius et al. 1993, 1996; Falconer 1994) and 1993 (SERTS-93; Brosius et al. 1996, 1997a, 1997b) carried a multilayer-coated diffraction grating that enhanced the instrumental efficiency in the first-order wavelength range, while the version flown in 1995 (SERTS-95; Brosius, Davila, & Thomas 1998a, 1998b; Brosius, Thomas, & Davila 1999) incorporated a multilayer grating that enhanced the instrumental sensitivity in the second-order waveband ($\sim$170–225 Å). This enhancement brought out many lines that were not seen during any of the previous flights and allowed them to be measured with the highest spectral resolution ever achieved for spatially resolved active region and quiet-Sun spectra in this wavelength range ($\sim$30 mÅ).

The version of SERTS flown on 1997 November 18 recorded spectrographic data on an intensified CCD detector with an array of 3072 $\times$ 2048 9 μm pixels. Its spectral bandpass was 299–353 Å with a measured resolution (instrumental FWHM) of 115 mÅ. It incorporated the same multilayer-coated toroidal diffraction grating that was flown in 1991 and 1993, which enhanced the instrumental sensitivity in this wavelength range over that of a standard gold-coated grating by factors up to 9. The spatial resolution was about 7″. SERTS-97 simultaneously recorded high-resolution spectra along a 6′ slit, and spectroheliograms of two 3′ $\times$ 8.′5 areas on each end of the slit (see Fig. 1).

An end-to-end radiometric calibration of the SERTS-97 instrument was performed at the Rutherford-Appleton Laboratory, UK, in the same facility used to calibrate the CDS experiment on *SOHO* and using the same EUV light source recalibrated by the Physikalisch-Technische Bundesanstalt against the synchrotron radiation of the BESSY I (a primary radiation standard). This was the first time that the SERTS instrument underwent an absolute radiometric calibration while fully assembled. The uncertainty on the absolute radiometric calibration is 15% and has been included in our calculations of the net uncertainties on emission-line intensities in Table 1. Coordinated, cospatial, time-invariant SERTS-97 and CDS spectra were used to carry out an intensity cross calibration that yielded an improved sensitivity curve for the CDS Normal Incidence Spectrometer's (NIS1) waveband (Thomas et al. 1999, 2000, in preparation).

Pre- and postflight wavelength calibrations were carried out at GSFC using EUV spectra of a hollow-cathode gas-discharge lamp emitting He II and Ne II lines with rest wavelengths known to better than 0.3 mÅ (Kaufman & Edlen 1974). Although the wavelength scale itself remained constant for the pre- and postflight laboratory wavelength calibrations, the zero point of this scale shifted slightly, indicating a small, constant offset between the in-flight wavelength scale and those measured in the laboratory. This translates into a small, systematic, unknown constant error on every wavelength measured from each area observed on the Sun. Fortunately, systematic wavelength shifts introduced by this offset are eliminated (directly canceled) by treating *relative* wavelength shifts between two different physical areas. In other words, because wavelengths that are measured simultaneously in any two different areas on the Sun include the same systematic shift, this shift is eliminated by subtracting the two wavelengths. Because the He II line at 303.78 Å is strong in both the laboratory and the solar spectra, we use it as the reference wavelength on which the solar spectrum is fixed to the laboratory wavelength scale. Thus, we set the He II wavelength in our solar "quiet edge" spectrum (the southernmost 19% of the slit in Fig. 1; see also Brosius et al. 2000) equal to its laboratory rest wavelength of 303.7822 Å and base all other wavelengths in this and the active region spectrum on this choice. Of course, this solar line could in fact be significantly Doppler shifted relative to its rest value, which would impose an additional systematic offset on all measured wavelengths. However, this offset too is eliminated from the *relative* wavelength shifts by subtraction. The He II active region average wavelength of 303.788 Å is listed in Table 1 indicates a statistically significant redshift relative to the "quiet edge" corresponding to a Doppler velocity of $\sim +5$ km s^{-1}. Brosius et al. (2000) report measurements of spatially resolved relative Doppler velocities for this and other strong lines in the SERTS-97 active region spectra; for example, the He II line yields a maximum relative redshift that corresponds to a Doppler velocity of $\sim +13$ km s^{-1} and a maximum relative blueshift that corresponds to a Doppler velocity of ~ -3 km s^{-1}, while the Fe XVI line at 335.40 Å yields corresponding values of $\sim +13$ and ~ -5 km s^{-1}, and the Fe XIV line at 334.17 Å yields corresponding values of $\sim +10$ and ~ -10 km s^{-1}.

In this paper we present and analyze the spatially averaged, absolutely calibrated SERTS-97 active region spectrum. Section 2 describes the SERTS-97 observations and data reduction procedures; § 3 presents the active region emission-line catalog; § 4 derives the physical quantities of the active solar corona such as density, differential emission measure (DEM), and nonthermal velocity; § 5 summarizes our findings.

2. OBSERVATIONS AND DATA REDUCTION

SERTS was launched on a Terrier-boosted Black Brant rocket from White Sands, New Mexico, at 1935 UT on 1997 November 18. It reached a maximum altitude of 332 km and recorded spectrographic data for nearly 400 s. Spectroheliograms of NOAA Active Region 8108 (N21°, E18°) and slit spectra of quiet areas south and slightly west of this region were obtained in the first pointing position. Slit spectra of AR 8108 and spectroheliograms of quiet areas to the northeast and southwest were obtained in the second pointing position. The SERTS field of view in the second pointing position is shown in Figure 1. The absolute pointing of the instrument was derived by co-aligning the 3′ $\times$ 8.′5 He II λ304 spectroheliograms with coordinated, full-disk He II λ304 images from the *SOHO*/Extreme-Ultraviolet Imaging Telescope (EIT), which could be done to an accuracy of 1.″8.

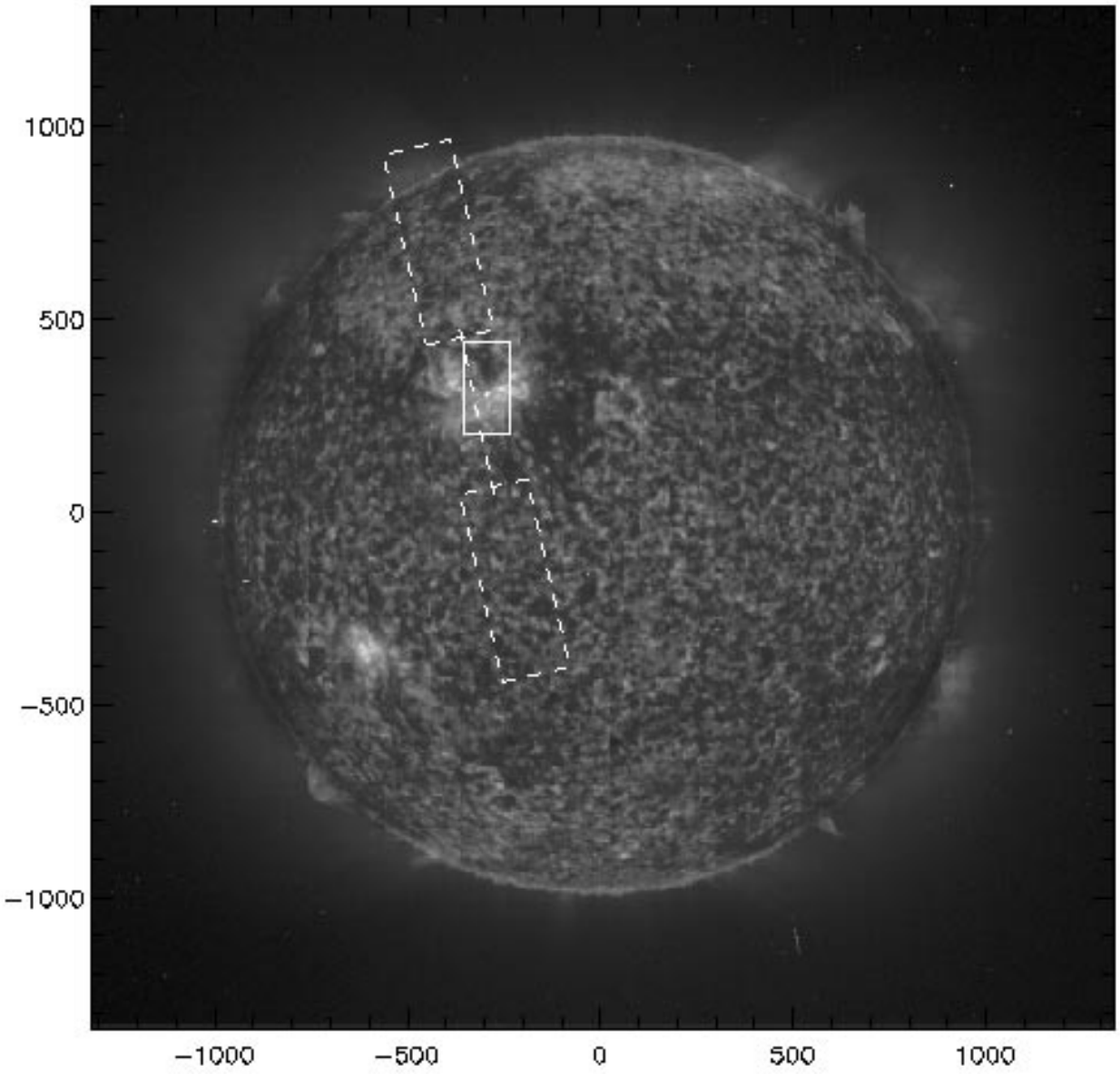

FIG. 1.—*SOHO*/EIT full-disk He II λ304 image obtained during the SERTS rocket flight on 1997 November 18. The dashed rectangles outline the 3′ × 8.′5 areas within which SERTS spectroheliograms were obtained, and the dashed line connecting them shows the location of the 7″ × 6′ SERTS slit. The solid rectangle shows the 2′ × 4′ CDS field of view, centered on NOAA AR 8108. Solar north is at the top. The tick marks indicate distance from disk center in arcseconds.

A total of 15 exposures were taken in the second pointing position at exposure times ranging from 1 to 60 s. Each of these was individually reduced by dark image subtraction and flat-field division using appropriate laboratory images that were obtained just before or after flight. Sections of each full image containing narrow slit data were extracted and aligned so that any vertical pixel gave measurements of the same solar source location for all wavelengths. In addition, a slight nonlinearity in the detector response was corrected. Data were then smoothed by 2 pixel averaging in the spatial direction and median filtered.

We examined the spatial variation of the He II λ303.78 line centroid wavelength in laboratory spectra as well as in the spatially resolved quiet-Sun spectra from the first SERTS pointing position and found that the wavelength varies systematically from one end of the slit to the other. The effect is somewhat more pronounced in the laboratory spectra than it is in the quiet-Sun spectra. We fit the systematic wavelength shift with a second-order polynomial and used this polynomial to remove the systematic trend from the active region spectra in the second SERTS pointing position (Brosius et al. 2000).

Since there was no significant time variability in the solar active region during this 332 s observing sequence, the nonsaturated portions of all 15 exposures were combined, taking into account the modeled wavelength-dependent atmospheric extinction for each one. Instrumental line shape distortions were reduced by two iterations of the Richardson-Lucy deconvolution technique (Richardson 1972; Lucy 1974). The instrumental point-spread function used in that procedure was derived from laboratory measurements of the He II line at 303.78 Å, which were taken with the SERTS-97 spectrograph just after its flight.

The resulting data set consists of imaged spectra in 222 1.″6 spatial pixels, each with 2830 19.8 mÅ wide spectral elements. Of that set, the 42 spatial pixels in the southern-

TABLE 1

SERTS-97 Absolutely Calibrated Active Region Line List

Wavelength (Å)	Intensity (ergs cm^{-2} s^{-1} sr^{-1})	FWHM[a] (mÅ)	Ion	Fractional Portion of λ (Å)				Note
				Flare[b]	Active[c]	Full[d]	Quiet[e]	
299.553	34.7 ± 11.5	162.1 ± 7.5	S XII	.50	.534	...	...	
300.440	23.0 ± 10.1	152.9 ± 7.5	...	...	.448	...	...	1
301.443	24.8 ± 9.9	146.4 ± 7.5	...	...	...	...	...	
302.322	37.3 ± 10.3	135.5 ± 7.5	Fe XV	...	.288	...	...	1, 2
302.923	15.1 ± 7.3	110.7 ± 7.5	...	...	...	...	...	
303.323	2340.0 ± 370.0	147.0 ± 7.5	Si XI	.33	.324	.325	...	
303.788	27,700.0 ± 4400.0	137.7 ± 7.5	He II	.79	.784	.782	...	
304.873	102.0 ± 18.0	128.1 ± 7.5	Fe XV	.80	.874	.853	...	2, 3
305.787	27.5 ± 10.3	152.8 ± 7.5	...	...	.842	...	...	1, 4
306.809	22.4 ± 9.4	150.0 ± 7.5	...	...	...	...	...	5
306.971	6.7 ± 3.9	63.1 ± 7.5	...	...	...	...	...	
307.764	43.1 ± 11.1	154.1 ± 7.5	Fe XV	.76	...	...	...	2
308.138	14.3 ± 7.5	127.6 ± 7.5	...	...	...	...	...	
308.548	33.8 ± 9.6	142.2 ± 7.5	Fe XI	.54	.575	.544	.515	
308.669	6.2 ± 4.0	68.2 ± 7.6	...	...	...	...	...	
308.991	29.1 ± 11.3	187.9 ± 7.5	...	.96	...	...	.972	1
309.229	14.7 ± 7.2	124.3 ± 7.5	...	.24	.205	...	...	1
309.632	13.2 ± 6.3	109.9 ± 7.5	...	...	...	...	.690	
310.580	11.7 ± 8.9	165.3 ± 7.6	...	...	...	...	...	
311.583	16.4 ± 7.4	135.4 ± 7.5	Fe XIII	...	.555	.552	.476	
311.769	20.9 ± 6.0	95.8 ± 7.5	Mg VIII	.74	.778	.77	.750	
312.172	61.6 ± 12.0	137.2 ± 7.5	Fe XIII	.18	.174	.164	...	
312.479	28.0 ± 7.7	122.6 ± 7.8	C IV	...	.429	.415	.368	
312.566	51.7 ± 10.5	123.9 ± 7.6	Fe XV	.57	.554	...	...	2
312.897	33.5 ± 7.9	115.7 ± 7.5	Fe XIII	...	.868	...	...	6
313.734	71.5 ± 13.4	153.8 ± 7.5	Mg VIII	.74	.736	.734	.758	
314.358	36.8 ± 8.5	131.6 ± 7.5	Si VIII	.31	.345	.350	.378	
314.601	14.7 ± 7.2	147.9 ± 7.6	...	...	.592	...	...	1
315.022	183.0 ± 30.0	159.1 ± 7.5	Mg VIII	.02	.024	.020	.019	
315.184	9.0 ± 4.5	95.3 ± 7.7	...	...	...	...	...	
315.322	10.6 ± 7.7	170.2 ± 8.3	...	...	...	...	...	
316.097	27.0 ± 6.4	108.6 ± 7.5	...	...	.129	...	...	
316.208	71.1 ± 12.8	143.2 ± 7.5	Si VIII	.19	.220	.216	.215	
316.498	4.8 ± 3.8	87.7 ± 7.6	...	...	.597	...	...	
317.017	34.8 ± 8.4	155.3 ± 7.5	Mg VIII	.02	.008	.01	.028	
317.252	8.8 ± 5.1	122.5 ± 7.7	...	...	...	...	...	
317.477	13.4 ± 8.7	213.8 ± 9.1	...	...	...	...	...	
317.640	3.6 ± 3.1	77.8 ± 7.8	Fe XV	.61	...	...	...	2
318.125	64.7 ± 11.6	143.4 ± 7.5	Fe XIII	.12	.120	.14	...	
319.026	55.9 ± 10.5	161.1 ± 7.5	Mg VII	.03	.023	...	.049	7
319.390	5.1 ± 3.6	100.0 ± 7.7	...	...	...	...	.457	
319.841	91.2 ± 15.3	149.2 ± 7.5	Si VIII	.84	.839	.830	.840	
320.247	11.4 ± 4.9	140.4 ± 7.6	...	...	...	...	...	1
320.559	85.3 ± 14.3	140.1 ± 7.5	Ni XVIII	.55	.558	...	...	
320.807	118.0 ± 19.0	140.4 ± 7.5	Fe XIII	.80	.800	.800	.903	8
321.003	7.5 ± 3.7	113.3 ± 7.6	...	.04	...	...	.903	8
321.475	28.7 ± 6.0	131.8 ± 7.5	Fe XIII	.47	.463	...	.436	
321.787	23.4 ± 5.3	130.5 ± 7.5	Fe XV	.78	.782	...	...	2
321.957	6.1 ± 4.2	146.1 ± 8.4	...	...	...	...	.991	
322.729	22.1 ± 7.3	249.2 ± 8.4	...	.72	.696	...	.695	
322.906	5.9 ± 3.7	138.4 ± 8.5	...	...	...	...	...	
324.975	7.8 ± 3.6	153.4 ± 7.7	Fe XV	.97	...	...	...	2
325.389	5.5 ± 2.9	128.6 ± 7.8	...	.40	.415	...	.312	9
325.781	2.8 ± 1.8	81.7 ± 7.8	...	...	...	...	...	
326.323	8.3 ± 2.8	121.9 ± 7.6	...	.36	.351	...	.357	
327.032	74.4 ± 12.1	146.4 ± 7.5	Fe XV	.03	.030	.02	...	2
327.850	5.5 ± 2.4	117.5 ± 7.7	...	.86	...	...	.771	
328.257	62.9 ± 10.3	147.9 ± 7.5	Cr XIII	.26	.259	...	.249	9
328.474	2.0 ± 1.6	83.1 ± 8.1	...	...	...	...	...	
328.751	3.0 ± 2.3	121.4 ± 8.3	...	...	...	...	.783	
329.916	11.2 ± 3.3	157.4 ± 7.6	...	.92	...	...	.892	

TABLE 1—*Continued*

Wavelength (Å)	Intensity (ergs cm^{-2} s^{-1} sr^{-1})	FWHM[a] (mÅ)	Ion	Fractional Portion of λ (Å)				Note
				Flare[b]	Active[c]	Full[d]	Quiet[e]	
330.218	8.6 ± 3.2	164.9 ± 7.8	...	.17	...	...	...	
330.994	6.2 ± 3.6	201.1 ± 8.3	Fe XV	.03	.072	...	...	2, 10
332.263	2.0 ± 1.5	83.6 ± 8.1	...	...	...	...	...	
332.784	112.0 ± 18.0	156.1 ± 7.5	Al X	.79	.782	.77	.785	
333.694	4.0 ± 2.2	124.0 ± 8.0	...	.74	...	...	...	
334.173	554.0 ± 89.0	134.9 ± 7.5	Fe XIV	.17	.171	.171	.174	
334.951	58.1 ± 10.7	350.0 ± 7.6	...	...	.043	...	...	11
335.404	5020.0 ± 804.0	133.8 ± 7.5	Fe XVI	.40	.401	.403	...	
337.226	9.5 ± 3.3	171.8 ± 7.7	...	.23	.238	...	.256	
338.273	57.6 ± 9.5	139.2 ± 7.5	Fe XII	.27	.273	.263	.260	
338.997	29.7 ± 5.4	145.9 ± 7.5	Mg VIII	.00	.000	...	.995	
339.822	10.1 ± 4.3	219.7 ± 7.9	...	...	...	...	.891	12
341.129	37.9 ± 6.6	149.4 ± 7.5	Fe XI	.12	.114	.112	.152	
341.285	3.7 ± 2.1	104.4 ± 8.2	...	...	...	...	...	
341.971	28.3 ± 5.2	136.3 ± 7.5	Si IX	.98	.974	.949	.952	
342.145	5.0 ± 1.9	87.2 ± 7.6	...	...	...	...	...	13
342.435	7.3 ± 3.1	147.6 ± 7.7	Ca VII	...	.390	...	.454	14
343.928	1.7 ± 1.6	78.2 ± 8.5	...	...	...	...	...	
344.082	13.0 ± 4.4	190.1 ± 7.9	...	.08	.080	...	.181	
344.987	16.7 ± 4.1	150.0 ± 7.8	Si IX	...	.958	...	.104	
345.138	65.7 ± 10.9	145.5 ± 7.5	Si IX	.13	.130	.13	.104	
345.735	57.0 ± 9.6	135.4 ± 7.5	Fe X	.73	.735	.739	.716	
346.849	77.9 ± 12.8	150.4 ± 7.5	Fe XII	.86	.857	.852	.858	
347.401	187.0 ± 30.0	142.4 ± 7.5	Si X	.41	.406	.402	.402	
347.848	17.2 ± 6.3	240.8 ± 7.7	Fe XVII	.85	.814	...	.878	15
348.179	170.0 ± 27.0	139.8 ± 7.5	Fe XIII	.18	.182	.184	.148	
349.032	7.5 ± 2.5	84.3 ± 7.6	Fe XI	...	.035	...	...	16
349.149	60.4 ± 10.4	173.7 ± 7.5	Mg VI	.13	.162	...	.148	17
349.871	121.0 ± 20.0	147.1 ± 7.5	Si IX	.88	.872	.874	.856	
350.489	18.9 ± 5.9	193.8 ± 7.6	Fe XVII	...	.477	...	...	
351.114	16.7 ± 4.9	155.2 ± 7.6	Mg V	...	.117	...	.196	18
351.696	4.8 ± 2.8	98.3 ± 7.7	...	...	...	...	.674	
352.112	171.0 ± 27.0	146.1 ± 7.5	Fe XII	.10	.106	.107	.111	
352.674	136.0 ± 22.0	134.5 ± 7.5	Fe XI	.68	.672	.670	.671	

Notes.—(1) May correspond to one of the highly uncertain He I wavelengths listed by Kelly 1987: 300.6, 302.4, 304.5, 305.4, 305.8, 309.1, 311.2, 314.6, 320.29, 338.1, and 344.7 Å. (2) Fe XV identification supported by laboratory wavelength measurements of Churilov et al. 1985, including lines at 302.334, 304.894, 307.730, 312.556, 317.597, 321.771, 324.975, 327.024, and 331.083 Å. (3) Brosius et al. 1999 report an unidentified line at 304.879 Å in laboratory wavelength calibration spectra containing emission lines of He I, He II, Ne II, and Ne III. Line intensity ratios (see text) suggest that this line in the solar spectrum is due predominantly to Fe XV. (4) Thomas & Neupert 1994 identify this line as Cr XII. Kelly 1987 lists six O III lines at nearby wavelengths. (5) Kelly 1987 lists O IV lines at wavelengths of 306.623 and 306.884 Å. (6) Brickhouse, Raymond, & Smith 1995 and Young et al. 1998 support this identification. (7) Possibly blended with an Fe XV line at 319.047 Å, measured in laboratory spectra by Churilov et al. 1985. (8) The wavelength reported by Brooks et al. is a blend of Fe XIII at 320.80 Å and Mg IV at 320.99 Å. (9) Brooks et al. identify this as a blend of Al VIII lines. (10) Although the Kelly (1987) list suggests possible blending with lines of Al VIII at 330.982 and 331.01 Å, this blending is probably ruled out because of the lack of detection of these Al VIII lines by Brooks et al. (despite the fact that they report the detection of other Al VIII lines). (11) Kelly 1987 suggests this broad component is a possible blend of Si VIII λ334.94, Al VIII λ334.951, and Fe XII λ335.06. (12) Kelly 1987 suggests that this broad component is a possible blend of lines from various ionization stages of Ca; Brooks et al. attribute this line to Ca VII. (13) Kelly 1987 suggests several possible constituents, including Mg VIII and a line from an unknown ionization stage of Si. (14) Kelly 1987 indicates a possible blend with Ca IV λ342.447. (15) This line is observed (but unidentified) in the quiet-Sun spectrum of Brooks et al., suggesting that the relatively broad line observed in the active region spectrum is blended with a component from an ion cooler than Fe XVII. (16) Identification based on Thomas & Neupert 1994 and CHIANTI database. (17) This broad feature is a blend of four Mg VI lines. (18) Possibly blended with a Cr XIII line at 351.16Å (Kelly 1987).

[a] Measured width, including instrumental, thermal, and nonthermal contributions.

[b] Dere 1978.

[c] Thomas & Neupert 1994.

[d] Behring et al. 1976.

[e] Brooks et al. 1999, in which the shortest wavelength is 308.515 Å.

most 67″ (19%) of the slit were used to obtain the average "quiet edge" spectrum against which Brosius et al. (2000) measured relative Doppler velocities as a function of position across the active region. For the average active region spectrum presented here, we incorporated only spectra from within a 221″ (139 spatial pixels or 63% of the SERTS slit) segment.

Each SERTS spectrum exhibits a background level because of dark current, scattered light, and actual solar continuum. We calculated this background for the averaged active region spectrum by removing emission lines from the initial spectrum, replacing them with appropriate local averages, and smoothing the remainder. The average background derived in this way was then subtracted from the

initial spectrum, leaving only an emission-line spectrum (with noise) on a zero base level. It should be pointed out that the spectral background is not known a priori and that the selection of lines to remove in order to determine the background is, to some extent, subjective. Not every bump and wiggle in a spectrum is necessarily a line; some may be noise.

3. ACTIVE REGION SPECTRUM

Figure 2 shows the SERTS-97 absolutely calibrated, background corrected, average active region spectrum of AR 8108. Emission lines in this spectrum were fitted with Gaussian profiles using the SolarSoft line fitting procedures XCFIT and CFIT_BLOCK. These yield the centroid wave-

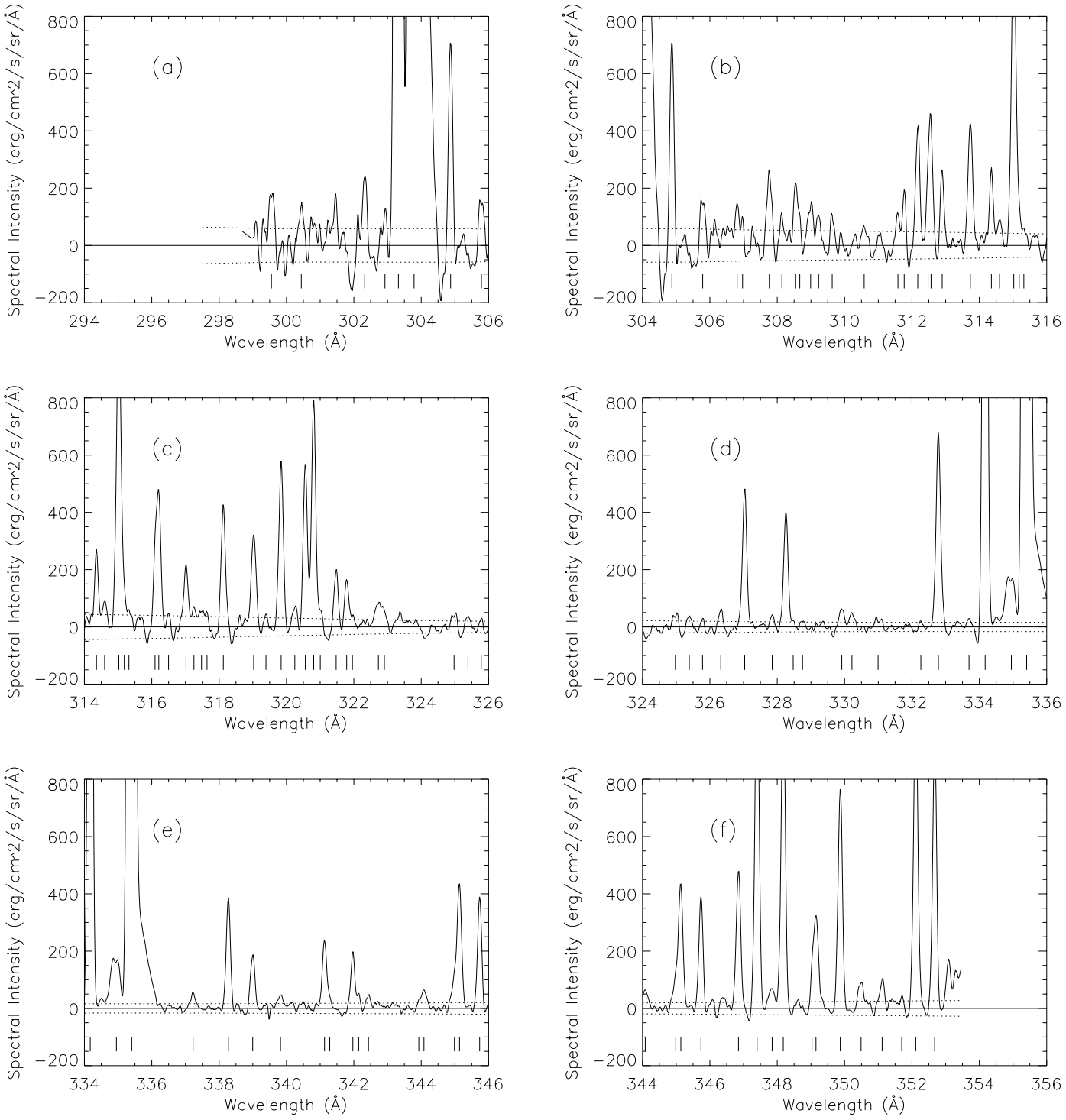

FIG. 2.—Frames *a–f* all show portions of the SERTS-97 background-corrected average active region spectrum. Lines that appear off-scale are not saturated; the vertical scale was chosen to enhance the visibility of weak lines. The uncertainty in the background is plotted as a dotted line above and below the zero base level. The tick marks indicate emission lines, listed in Table 1, whose profiles have been fit with Gaussians.

length, the profile amplitude, and the FWHM. Corresponding statistical uncertainties, most of which are relatively small, were obtained with CFIT_BLOCK_ERROR. The amplitude and FWHM were used to derive integrated line intensities. Lines fitted in this way are indicated by tick marks at the fitted centroid wavelengths. A horizontal line at zero intensity is shown for reference. The uncertainty in the active region spectral background is also shown (as a dotted line) and included in our calculations of the net uncertainties on emission-line intensities. Weaker lines are much more susceptible to background uncertainties than stronger lines, as is evident in their relatively greater associated uncertainties.

Table 1 lists 95 emission lines observed in Figure 2. The table includes measured wavelength (in Å), integrated intensity (in ergs cm^{-2} s^{-1} sr^{-1}) with a 1 σ measurement uncertainty (which includes statistical, background, and 15% absolute calibration uncertainties), FWHM with a 1 σ measurement uncertainty (in mÅ), line identifications, and corresponding wavelengths (stripped of their first three digits) from four other references for comparison: the flare spectrum of Dere (1978), the active region spectrum of Thomas & Neupert (1994), the full-Sun spectrum of Behring et al. (1976), and the quiet-Sun spectrum of Brooks et al. (1999). Notes to the table include references to the Kelly (1987) Finding List, a compilation of laboratory, solar, and theoretical wavelengths that has proved to be an extremely valuable tool for identifying lines in solar EUV spectra. Brooks et al. (1999) present an average quiet-Sun spectrum obtained with the NIS1/CDS on *SOHO*; they observe no lines from ionization stages of iron greater than XIV.

Available density- and temperature-insensitive line intensity ratios (hereafter "insensitive ratios") confirm the accuracy of the SERTS-97 relative radiometric calibration. The use of such ratios was proposed by Neupert & Kastner (1983) as a means of monitoring relative calibration variations of in-flight EUV spectrometers and was applied by Brosius et al. (1998a, 1998b) to derive the relative radiometric calibration for SERTS-95 from active region and quiet-Sun spectra. The insensitive ratios used in this work should also be helpful for ongoing CDS calibration efforts.

For the present work we used CHIANTI (Dere et al. 1997) version 2.0 (Landi et al. 1999) to obtain theoretical values of insensitive ratios among emission lines observed by SERTS-97. These include lines from Fe XI, XII, XIII, and XV, as well as Mg VIII, Si VIII, and Si IX. The ratios are listed in Table 2, in which the first column identifies the ion and wavelengths, the second column provides the theoretical ratios (using energy units), and the third column gives the measured value from the SERTS-97 average active region spectrum. Some of the theoretical insensitive ratios exhibit slight variations with density. In those cases the insensitive ratio itself is taken to be the average of the maximum and minimum values within the range $9.0 \leq \log n_e \leq 10.0$, and the uncertainty is half the difference between those same values. In each case the intensity ratios were calculated at the temperature of maximum ion abundance T_{max} (i.e., the lines' "formation temperature") using the Mazzotta et al. (1998) ionization equilibrium calculations. (We also derived theoretical values of insensitive ratios using the ionization equilibrium calculations of Arnaud & Rothenflug 1985 and Arnaud & Raymond 1992 but found only a few differences from the values listed in Table 2, the largest being 0.003. The differences occur only in nonbranching ratios for ions whose T_{max} varies among the different sets of ionization equilibrium calculations.) Table 2 reveals that all but two of the measured ratios from the active region spectrum agree with their corresponding theoretical values within the measurement uncertainties; the two discrepant ratios (Mg VIII $\lambda\lambda$317.0/315.0 and $\lambda\lambda$339.0/315.0) agree within factors of 1.5 times their measurement uncertainties. The theoretical values for these ratios have varied somewhat over time (e.g., Bhatia & Thomas 1998 and various versions of CHIANTI), so it is not unlikely that additional theoretical improvements will be forthcoming.

TABLE 2

CONFIRMATION OF THE SERTS-97 CALIBRATION WITH INSENSITIVE RATIOS

LINE RATIO	THEORETICAL	MEASURED
Fe XI $\lambda\lambda$341.1/352.7	0.278 ± 0.021	0.280 ± 0.067
Fe XII $\lambda\lambda$346.8/352.1	0.517	0.456 ± 0.105
Fe XIII $\lambda\lambda$321.4/312.1	0.500	0.466 ± 0.133
Fe XIII $\lambda\lambda$312.9/320.8	0.291 ± 0.033	0.284 ± 0.081
Fe XIII $\lambda\lambda$320.8/311.5	7.23	7.20 ± 3.46
Fe XV $\lambda\lambda$312.5/327.0	0.590	0.695 ± 0.181
Mg VIII $\lambda\lambda$313.7/315.0	0.353 ± 0.007	0.391 ± 0.097
Mg VIII $\lambda\lambda$317.0/315.0	0.250 ± 0.005	0.188 ± 0.054
Mg VIII $\lambda\lambda$339.0/315.0	0.228 ± 0.002	0.163 ± 0.040
Mg VIII $\lambda\lambda$339.0/317.0	0.916 ± 0.012	0.853 ± 0.258
Si VIII $\lambda\lambda$314.3/316.2	0.529	0.518 ± 0.152
Si VIII $\lambda\lambda$314.3/319.8	0.349 ± 0.001	0.404 ± 0.115
Si IX $\lambda\lambda$344.9/345.1	0.257 ± 0.008	0.254 ± 0.075
Si IX $\lambda\lambda$341.9/345.1	0.451 ± 0.014	0.431 ± 0.107
Si IX $\lambda\lambda$344.9/341.9	0.570	0.590 ± 0.181

NOTE.—Theoretical values are derived with data from CHIANTI version 2.0 (Landi et al. 1999) and correspond to the average ratio at densities of 10^9 and 10^{10} cm^{-3}; uncertainty is half the difference between the two.

Nine of the Fe XV emission lines observed in the laboratory spectrum of Churilov et al. (1985), at wavelengths of 302.334, 304.894, 307.730, 312.556, 317.597, 321.771, 324.975, 327.024, and 331.083 Å, are found in our solar active region spectrum. This indicates a likely association of our observed solar lines with Fe XV. The agreement between laboratory and solar wavelengths is fairly good, although the former may include shifts due to plasma expansion and optical depth effects, while the latter may include shifts due to mass motions and a small, undetermined offset. All of these lines have been observed in previous solar spectra, but they have not all previously been associated with Fe XV, and they have not all previously been observed simultaneously in a well-calibrated spectrum. The present observations, therefore, provide a unique data set that may be used to derive and improve atomic parameters for this ion. In particular, we note that the CHIANTI wavelengths closest to the measured solar wavelengths of 302.32 and 304.87 Å are 0.1 Å or more greater, at 302.42 and 305.00 Å. Kelly (1987) lists values of 302.45 and 305.00 Å for these same lines. Agreement between the measured solar insensitive ratio Fe XV $\lambda\lambda$304.87/321.78 (4.37 ± 1.26) and its theoretical value (4.27 ± 0.36, where we have used the emissivity at the CHIANTI wavelength of 305.00 Å) supports our association of the λ304.87 line with Fe XV. (It also provides additional verification of the SERTS-97 relative radiometric calibration.) However, it should be pointed out that synthetic spectral data based on CHIANTI and the active region DEM (see § 4.3) suggest that ~20% of the intensity

observed at 304.87 Å is due to Mn XIV, while ~30% of the intensity observed at 321.78 Å is due to a mixture of Fe X and Ni XIII. Interestingly, we have observed an unidentified line at 304.879 Å in laboratory wavelength calibration spectra (Brosius et al. 1999) that contains numerous emission lines of He I, He II, Ne II, and Ne III (but not Fe XV or similarly hot ions like Mn XIV). This raises the question as to whether emission from this unidentified line in the laboratory spectra contributes to the solar emission observed at this wavelength.

The CHIANTI database includes an Fe XV line at 323.57 Å that theoretically should be ~10 times as intense as the Fe XV line at 324.97 Å. Since the λ323.57 line is not present in either the SERTS solar spectrum or the laboratory Fe XV spectrum, we concur with Keenan et al. (1993) that the λ323.57 line is not associated with Fe XV. The theoretical ratio of Fe XV λλ324.97/327.03 (derived using the closest matching wavelengths in the CHIANTI database) is density sensitive, varying from 0.00156 at $\log n_e = 9.0$ to 0.00278 at $\log n_e = 10.0$. The measured value of 0.105 ± 0.051, however, is not consistent with this. Inconsistencies between the observed and theoretical ratios noted by Young et al. (1998) led those authors to suggest that the λ324.97 line may not even be associated with Fe XV. Here we suggest that it may be blended with emission from other ion(s), or that the atomic physics need to be revised. The only Fe XV intensity ratio that we have included in our calibration verification (see Table 2) is that of λλ312.56/327.03, for which the atomic data are reliable and the blending minimal. Based on CHIANTI data, Co XVII contributes only 5% of the total intensity at 312.56 Å.

The widths listed in Table 1 are *measured* line widths: we have not removed the instrumental contribution. The instrumental width can be removed by using the simple relation among the intrinsic, measured, and instrumental widths: $\mathrm{FWHM}^2_{\mathrm{intrinsic}} = \mathrm{FWHM}^2_{\mathrm{measured}} - \mathrm{FWHM}^2_{\mathrm{instrumental}}$. Intensities of lines with widths narrower than instrumental (115 mÅ) are to be treated with caution. It is possible that some of the weak, narrow, unidentified lines (especially the ones that are not observed in any of the four other reference spectra) may be noise.

4. MEASUREMENT OF ACTIVE REGION PHYSICAL QUANTITIES

4.1. *Density*

Density-sensitive line intensity ratios are available for Fe XI, XII, XIII, and XV. Theoretical curves for these ions are derived from CHIANTI version 2.0 (Landi et al. 1999). Large variations in the theoretical ratios correspond to small uncertainties in the derived electron densities; small variations in the theoretical ratios yield undetermined electron densities. For Fe XI λλ308.55/352.67 we obtain a ratio of 0.249 ± 0.082, which yields $\log n_e = 9.92 \pm 0.28$ (where n_e is in cm^{-3}). For Fe XII λλ338.27/352.11 we obtain a ratio of 0.337 ± 0.078, which yields $\log n_e = 9.74 \pm 0.28$. For Fe XIII we note that Table 2 contains two different groups of insensitive ratios; the intensity ratio between the strongest members of the respective groups (λλ320.80/312.17) is 1.92 ± 0.49, which yields $\log n_e = 9.52 \pm 0.30$. The Fe XIII curve that exhibits the largest variation in theoretical ratio as a function of density is that of λλ318.12/348.18; its measured ratio of 0.381 ± 0.092 yields $\log n_e = 9.55 \pm 0.10$, which is consistent with the value derived from λλ320.80/312.17. The Fe XIII ratio λλ320.80/348.18 (0.696 ± 0.159) yields a significantly lower logarithmic density of 9.12 ± 0.12, which is not consistent with the density derived from the other two Fe XIII ratios above. For Fe XV λλ321.78/327.03, we obtain a ratio of 0.314 ± 0.088, which yields $\log n_e = 9.99 \pm 0.34$. Removing the 30% non–Fe XV contribution mentioned above from the line at 321.78 Å yields a revised Fe XV ratio of 0.220 ± 0.061, which provides $\log n_e = 9.62 \pm 0.26$.

4.2. *Nonthermal Velocities*

Pre- and postflight measurements of laboratory spectra generated with a hollow-cathode gas-discharge tube emitting EUV lines of He I–II and Ne II–III yield an instrumental width $F_{\mathrm{inst}} = 115$ mÅ that is independent of position along the SERTS slit. By removing this and the thermal width

$$F_{\mathrm{thermal}} = (\lambda/c)(2akT/m)^{1/2} \quad (1)$$

(where λ is the wavelength, c the speed of light, $a = 4 \ln 2$, k the Boltzmann constant, T the "formation" temperature, and m the atomic mass) from the measured width F_{meas} for any individual line, we obtain that line's nonthermal width

$$F^2_{\mathrm{nontherm}} = F^2_{\mathrm{meas}} - F^2_{\mathrm{inst}} - F^2_{\mathrm{thermal}} \, . \quad (2)$$

(We obtain $\log T_{\mathrm{max}}$ values of 5.98, 6.07, 6.13, 6.20, 6.28, 6.32, 6.42, and 6.54 for Fe X, XI, XII, XIII, XIV, XV, XVI, and Ni XVIII, respectively, by cubic spline interpolation on the ionization fraction calculations of Mazzotta et al. 1998.) The nonthermal width corresponds to a nonthermal velocity

$$V_{\mathrm{nontherm}} = (cF_{\mathrm{nontherm}})/(a^{1/2}\lambda) \, . \quad (3)$$

The uncertainty on this velocity is given by

$$\sigma_{V_{\mathrm{nontherm}}} = (V_{\mathrm{nontherm}}/F^2_{\mathrm{nontherm}}) \times (\sigma^2_{F_{\mathrm{meas}}} F^2_{\mathrm{meas}} + \sigma^2_{F_{\mathrm{inst}}} F^2_{\mathrm{inst}})^{1/2} \, , \quad (4)$$

where $\sigma_{F_{\mathrm{meas}}}$ is the uncertainty on the measured width, and $\sigma_{F_{\mathrm{inst}}}$ is the uncertainty on the instrumental width (1.4 mÅ). The uncertainty on the nonthermal width (velocity) becomes very large when the nonthermal width (velocity) itself becomes very small; this is because the relatively small uncertainty associated with the line's total measured width is eventually associated only with the nonthermal component. We applied the above expressions to the strongest line observed for each ionization stage of Fe from X through XVI and Ni XVIII (in Table 1) to obtain nonthermal velocities and corresponding uncertainties. Results are summarized in Figure 3. We plot the nonthermal velocities as a function of the ionization stage rather than the formation temperature because the former is a more robust quantity; formation temperatures may change with improved ionization balance computations.

Figure 3 shows that the nonthermal velocity for each ion is consistent with a value of 35 km s^{-1} (plotted as a dotted horizontal line). This value is somewhat higher than the ~20 km s^{-1} obtained by Davila et al. (2000 in preparation) and based on earlier SERTS data, but the result is qualitatively the same—nonthermal velocities for EUV lines of coronal ions (formed at $T \gtrsim 1 \times 10^6$ K) are consistent with a constant value regardless of formation temperature (ionization stage). Nonthermal velocities similarly calculated for the strongest lines of Si IX, X, and XI are also consistent with 35 km s^{-1}. Saba & Strong (1991) found nonthermal velocities of 42 ± 30, 58 ± 4, and 44 ± 4 km

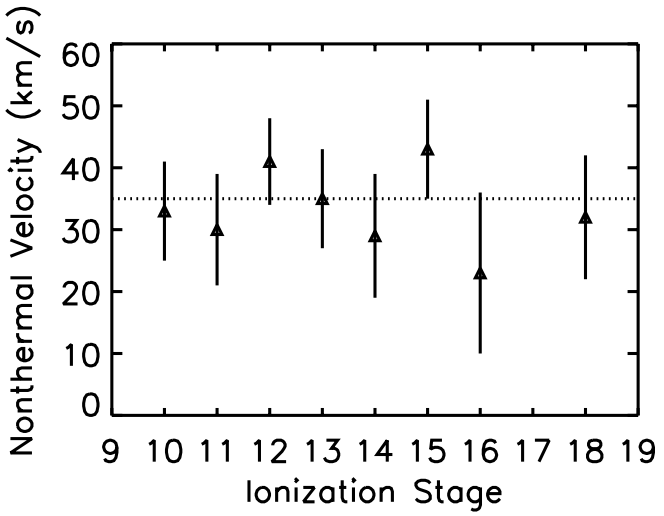

FIG. 3.—Nonthermal velocities derived from the strongest emission lines of Fe X–XVI and Ni XVIII in the active region spectrum as a function of ionization stage. Within the measurement uncertainties, all of the nonthermal velocities are consistent with a value of 35 km s^{-1}.

s^{-1} from lines of O VIII, Ne IX, and Mg XI, respectively, observed in active regions with the X-Ray Polychromator (XRP) on board the *Solar Maximum Mission*. Doyle et al. (1997) report Fe XII nonthermal velocities of 27 km s^{-1} from quiet-Sun limb spectra obtained with the High-Resolution Telescope and Spectrograph (HRTS) sounding rocket experiment. Chae, Schuhle, & Lemaire (1998) report nonthermal velocities of 23 ± 5 and 16 ± 7 km s^{-1} in Mg X and Fe XII lines observed in *SOHO*/SUMER quiet-Sun spectra.

4.3. *Differential Emission Measure*

The differential emission measure is a measure of the amount of emitting plasma along the line of sight within the temperature interval T to $T + dT$. A variety of methods have been developed for calculating the DEM, as described in Harrison & Thompson (1991) and references therein. In the present work we employ the method of Landi & Landini (1997), which adopts an iterative procedure and uses density-independent lines.

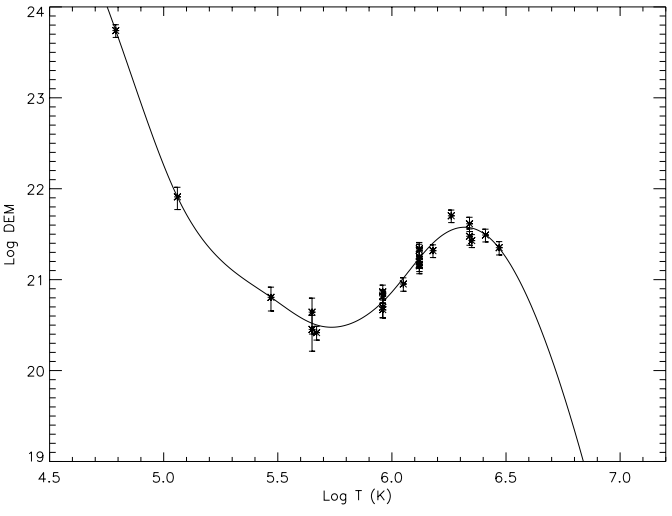

FIG. 4.—Differential emission measure obtained with the SERTS-97 average active region spectrum, using the method of Landi & Landini (1997), the CHIANTI Version 2.0 atomic physics database (Landi et al. 1999), the Mazzotta et al. (1998) ionization equilibrium computations, and the Feldman (1992) coronal element abundances. The spectral lines used to derive this DEM are listed in Table 3, along with their "effective" temperatures (at which they are plotted in the figure) and observed-to-theoretical intensity ratios.

The intensity emitted by a plasma in an optically thin line is given by

$$I_{ij} = \frac{1}{4\pi} \int_H N_j(X^{+m}) A_{ij} \Delta E_{ij} \, dh \text{ ergs cm}^{-2} \text{ s}^{-1} \text{ sr}^{-1} , \quad (5)$$

where $N_j(X^{+m})$ is the number density population of level j of ion X^{+m}, A_{ij} is the radiative probability to decay to level i, ΔE_{ij} is the energy of the transition, and integration is performed over height. Defining the contribution function as

$$G_{ij}(T, N_e) = \frac{N_j(X^{+m})}{N(X^{+m})} \frac{N(X^{+m})}{N(X)} \times \frac{N(X)}{N(H)} \frac{N(H)}{N_e} \frac{A_{ij}}{N_e} \Delta E_{ij} , \quad (6)$$

where the first term on the right is the relative population of the excited level j, the second term is the relative abundance of the ion X^{+m} (i.e., "ion fraction"), the third term is the abundance of the element relative to hydrogen, and the fourth term is the number density of hydrogen relative to the number density of electrons (≈ 0.8 for a completely ionized plasma of standard solar composition). Defining the DEM as

$$\varphi(T) = N_e^2 \frac{dh}{dT} , \quad (7)$$

the line intensity (eq. [5]) can be rewritten as

$$I_{ij} = \frac{1}{4\pi} \int_T G_{ij}(T, N_e) \varphi(T) dT . \quad (8)$$

In order to determine $\varphi(T)$ from a set of observed intensities that are emitted by ions formed at different temperatures, a trial DEM $\varphi_0(T)$ and its associated correction function $\omega(T)$ are adopted such that

$$\varphi(T) = \omega(T) \varphi_0(T) . \quad (9)$$

Inserting equation (9) for the DEM in equation (8) and assuming that the correction function is slowly varying as a function of the electron temperature, the correction function and an improved DEM are evaluated for "effective" temperatures (see Table 3) defined for each of the observed lines as in Landi & Landini (1997). The improved DEM is used as the new trial DEM for the next iteration, and the procedure is repeated until either the correction function is equal to unity within the measurement uncertainties or the minimum χ^2 is obtained. The contribution functions of the observed lines used in the present work were calculated using the CHIANTI database (Dere et al. 1997; Landi et al. 1999) adopting the ion fractions from Mazzotta et al. (1998) and the coronal element abundances from Feldman (1992). (White et al. 2000, using coordinated EUV observations obtained with CDS and radio observations obtained with the Very Large Array, derive a coronal iron abundance $Fe/H = 1.56 \pm 0.31 \times 10^{-4}$, which agrees with the Feldman 1992 value within the measurement uncertainties.)

The resulting DEM (Fig. 4; see also Table 3) shows a

TABLE 3

EMISSION LINES USED TO DERIVE ACTIVE REGION DEM

LINE	$T_{\rm eff}$ (K)[a]	$I_{\rm obs}/I^{\rm b}_{\rm dem}$
He II λ303.780	4.79	1.00 ± 0.15
C IV λ312.420	5.06	1.00 ± 0.25
Mg V λ351.088	5.47	1.00 ± 0.30
Ca VII λ342.395	5.66	0.86 ± 0.35
Ca VII λ339.966	5.66	1.33 ± 0.45
Mg VI λ349.163	5.68	0.82 ± 0.20
Mg VIII λ315.016	5.97	1.15 ± 0.20
Mg VIII λ313.744	5.97	1.28 ± 0.30
Mg VIII λ317.028	5.97	0.87 ± 0.20
Mg VIII λ338.984	5.97	0.82 ± 0.15
Fe X λ345.723	6.06	0.86 ± 0.20
Si IX λ349.873	6.13	0.92 ± 0.15
Si IX λ345.124	6.13	0.85 ± 0.15
Si IX λ341.949	6.13	0.83 ± 0.20
Si IX λ344.951	6.13	1.04 ± 0.25
Fe XI λ341.113	6.13	1.27 ± 0.25
Fe XI λ352.662	6.13	1.23 ± 0.25
Al X λ332.789	6.18	0.82 ± 0.20
Si XI λ303.324	6.26	1.44 ± 0.20
Fe XV λ304.999	6.34	1.10 ± 0.20
Fe XV λ312.539	6.35	0.80 ± 0.20
Fe XV λ327.011	6.36	0.73 ± 0.25
Fe XVI λ335.410	6.42	0.99 ± 0.15
Ni XVIII λ320.565	6.48	1.01 ± 0.15

NOTE.—These are the lines that were used to derive the DEM shown in Fig. 4. Wavelengths listed here are from the CHIANTI database.

[a] Effective temperature, as defined by Landi & Landini 1997. This is not the same as the formation temperature (the temperature of maximum ion abundance), for which examples derived from the Mazzotta et al. 1998 ion fraction calculations are given in § 4.2.

[b] Ratio of the observed intensity to the theoretical intensity derived from the DEM in Fig. 4, with measurement uncertainties.

broad maximum around 2×10^6 K, with a substantial amount of material up to 4×10^6 K. For higher temperatures, the DEM falls rapidly to zero, so that only a small amount of plasma hotter than 4×10^6 K is present. This is consistent with the results of Schmelz et al. (1999), who used coordinated SERTS-93 EUV spectra and *Yohkoh*/SXT broadband soft X-ray data to derive an active region DEM. Only a few lines are available at transition region temperatures, but they indicate a minimum around 5×10^5 K.

DEM analyses can be used to determine the relative abundances of elements whose lines are used to determine the DEM (e.g., Landi & Landini 1997, 1998). In the present work the Feldman (1992) coronal abundance of Si relative to Fe, Ni, Mg, and Al needed to be diminished by a factor of 1.7, while the coronal abundance of Ca needed to be increased by a factor of 2.8. Our abundance correction for Si is consistent with that reported by Landi & Landini (1998) for a variety of solar features. Our abundance correction for Ca is somewhat smaller than that derived by Landi & Landini (1998) and Del Zanna & Bromage (1999), possibly because of the different sets of ion fraction calculations adopted (Gianetti, Landi, & Landini 2000).

Gianetti et al. (2000) examined the differences among DEM curves that were derived from three different sets of ionization equilibrium computations. They computed and compared DEM curves for a solar active region observed with the *SOHO*/CDS based on the ion fraction calculations of Shull & Steenberg (1982a, 1982b), Arnaud & Rothenflug (1985, with Arnaud & Raymond 1992 for the Fe ions), and Mazzotta et al. (1998), and found that although the curves differ significantly in both shape and value, the differences are factors $\lesssim 2$ over most of the temperature range.

Except for He II and C IV, by far the coolest two ions in our sample, all of the ions used to determine the DEM have a low (<10 eV) first ionization potential (FIP). Thus, a direct comparison between coronal emission from low-FIP and high-FIP elements is not possible, and we cannot use the SERTS-97 observations to determine the relative abundances of low-FIP to high-FIP elements in the corona.

5. SUMMARY

We have presented a well-calibrated, high-resolution (instrumental FWHM of 115 mÅ) EUV spectrum of a solar active region obtained with the SERTS sounding rocket during its 1997 November 18 flight. The instrument incorporated an intensified CCD detector and a multilayer-coated toroidal diffraction grating with enhanced sensitivity over that of a standard gold-coated grating throughout the instrument's 299–353 Å spectral bandpass. Nearly 100 emission lines were observed. The absolute radiometric calibration of the rocket instrument, measured to an accuracy of 15% in the same facility used to calibrate CDS on *SOHO*, is confirmed by the excellent agreement between the measured and theoretical values of density- and temperature-insensitive line intensity ratios. Nine emission lines of Fe XV are identified in our spectrum; however, large differences between wavelengths in the CHIANTI database and some of the measured solar wavelengths, as well as inconsistencies of various theoretical intensity ratios, suggest a need for improvement in some of the Fe XV atomic physics parameters and/or the presence of unidentified blending lines. Density-sensitive line intensity ratios of Fe XI λλ308.55/352.67, Fe XII λλ338.27/352.11, Fe XIII λλ320.80/312.17, and Fe XV λλ321.78/327.03 yield logarithmic electron densities (in $\rm cm^{-3}$) of 9.92 ± 0.28, 9.74 ± 0.28, 9.52 ± 0.30, and 9.62 ± 0.26, respectively. Using the strongest emission line observed for each ionization stage of Fe from X through XVI and Ni XVIII, all of the measured nonthermal line widths yield velocities consistent with 35 km $\rm s^{-1}$. The differential emission measure curve derived from the observed line intensities exhibits a relative minimum at $\log T \sim 5.7$, a broad maximum centered around $\log T \sim 6.3$, and a rapid decline for temperatures above $\log T \sim 6.6$.

J. W. B. acknowledges NASA support through contract NAS 5-99145. J. M. D. and R. J. T. acknowledge NASA support for the SERTS program by RTOP grants from the Solar Physics Office of NASA's Space Physics Division.

REFERENCES

Arnaud, M., & Raymond, J. 1992, ApJ, 398, 394
Arnaud, M., & Rothenflug, R. 1985, A&AS, 60, 425
Behring, W. E., Cohen, L., Feldman, U., & Doschek, G. A. 1976, ApJ, 203, 521
Bhatia, A. K., & Thomas, R. J. 1998, ApJ, 497, 483
Brickhouse, N. S., Raymond, J. C., & Smith, B. W. 1995, ApJS, 97, 551
Brooks, D. H., et al. 1999, A&A, 347, 277
Brosius, J. W., Davila, J. M., & Thomas, R. J. 1998a, ApJ, 497, L113
———. 1998b, ApJS, 119, 255
Brosius, J. W., Davila, J. M., Thomas, R. J., & Monsignori-Fossi, B. C. 1996, ApJS, 106, 143
Brosius, J. W., Davila, J. M., Thomas, R. J., Saba, J. L. R., Hara, H., & Monsignori-Fossi, B. C. 1997a, ApJ, 477, 969
Brosius, J. W., Davila, J. M., Thomas, R. J., & White, S. M. 1997b, ApJ, 488, 488
Brosius, J. W., et al. 1993, ApJ, 411, 410
Brosius, J. W., Thomas, R. J., & Davila, J. M. 1999, ApJ, 526, 494
Brosius, J. W., Thomas, R. J., Davila, J. M., & Thompson, W. T. 2000, Sol. Phys., in press
Chae, J., Schuhle, U., & Lemaire, P. 1998, ApJ, 505, 957
Churilov, S. S., Kononov, E. Y., Ryabtsev, A. N., & Zayikin, Y. F. 1985, Phys. Scr., 32, 501
Del Zanna, G., & Bromage, B. J. I. 1999, J. Geophys. Res., 104, 9753
Dere, K. P. 1978, ApJ, 221, 1062
Dere, K. P., Landi, E., Mason, H. E., Monsignori-Fossi, B. C., & Young, P. R. 1997, A&AS, 125, 149
Dere, K. P., Mason, H. E., Widing, K. G., & Bhatia, A. K. 1979, ApJS, 40, 341
Doyle, J. G., O'Shea, E., Erdelyi, R., Dere, K. P., Socker, D. G., & Keenan, F. P. 1997, Sol. Phys., 173, 243
Dupree, A. K., Huber, M. C. E., Noyes, R. W., Parkinson, W. H., Reeves, E. M., & Withbroe, G. L. 1973, ApJ, 182, 321
Falconer, D. A. 1994, Ph.D. thesis, Univ. Maryland
Feldman, U. 1992, Phys. Scr., 46, 202
Gianetti, D., Landi, E., & Landini, M. 2000, A&A, 360, 1148
Harrison, R. A., & Thompson, A. M., eds. 1991, Intensity Integral Inversion Techniques: A Study in Preparation for the *SOHO* Mission RAL-91-092, RAL Tech. Rep.
Kaufman, V., & Edlen, B. 1974, J. Phys. Chem. Ref. Data, 3, 825
Keenan, F. P., Dufton, P. L., Conlon, E. S., Foster, V. J., Kingston, A. E., & Widing, K. G. 1993, ApJ, 405, 798
Kelly, R. L. 1987, J. Phys. Chem. Ref. Data, 16, S1
Landi, E., & Landini, M. 1997, A&A, 327, 1230
———. 1998, A&A, 340, 265
Landi, E., Landini, M., Dere, K. P., Young, P. R., & Mason, H. E. 1999, A&AS, 135, 339
Lucy, L. B. 1974, AJ, 79, 745
Malinovsky, M., & Heroux, L. 1973, ApJ, 181, 1009
Mazzotta, P., Mazzitelli, G., Colafrancesco, S., & Vittorio, N. 1998, A&AS, 133, 403
Neupert, W. M., Epstein, G. L., Thomas, R. J., & Thompson, W. T. 1992, Sol. Phys., 137, 87
Neupert, W. M., & Kastner, S. O. 1983, A&A, 128, 181
Neupert, W. M., Thomas, R. J., & Chapman, R. D. 1974, Sol. Phys., 34, 349
Richardson, W. H. 1972, J. Opt. Soc. Am., 62, 55
Saba, J. L. R., & Strong, K. T. 1991, ApJ, 375, 789
Schmelz, J. T., Saba, J. L. R., Strong, K. T., Winter, H. D., & Brosius, J. W. 1999, ApJ, 523, 432
Shull, J. M., & Van Steenberg, M. 1982a, ApJS, 48, 95
———. 1982b, ApJS, 49, 351
Thomas, R. J., Davila, J. M., Thompson, W. T., Kent, B. J., & Hollandt, J. 1999, BAAS, 194, 16.06
Thomas, R. J., & Neupert, W. M. 1994, ApJS, 91, 461
Tousey, R., Bartoe, J.-D. F., Brueckner, G. E., & Purcell, J. D. 1977, Appl. Opt., 16, 870
Vernazza, J. E., & Reeves, E. M. 1978, ApJS, 37, 485
White, S. M., Thomas, R. J., Brosius, J. W., & Kundu, M. R. 2000, ApJ, 534, L203
Young, P. R., Landi, E., & Thomas, R. J. 1998, A&A, 329, 291